

# The role of stochastic Fermi-type particle acceleration in the inner jets of Active Galactic Nuclei

JIESHUANG WANG,<sup>1</sup> FRANK M. RIEGER,<sup>2,3,1</sup> AND YOSUKE MIZUNO<sup>4,5</sup>

<sup>1</sup>*Max-Planck-Institut für Kernphysik, Saupfercheckweg 1, D-69117 Heidelberg, Germany*

<sup>2</sup>*Max Planck Institute for Plasma Physics, Boltzmannstraße 2, D-85748 Garching, Germany*

<sup>3</sup>*Institute for Theoretical Physics, University of Heidelberg, Philosophenweg 12, D-69120 Heidelberg, Germany*

<sup>4</sup>*Tsung-Dao Lee Institute, Shanghai Jiao Tong University, 520 Shengrong Road, Shanghai, 201210, China*

<sup>5</sup>*School of Physics & Astronomy, Shanghai Jiao Tong University, 800 Dongchuan Road, Shanghai, 200240, China*

## ABSTRACT

High-resolution radio observations of nearby active galactic nuclei have revealed extended, limb-brightened structures in their inner jets. This ties in with other multi-wavelength observations from radio to X-ray and gamma-ray, indicating that a structured jet model is required. While electrons need to be kept energized to account for the observed features, the underlying particle acceleration mechanism is still unclear. We explore the role of stochastic Fermi-type particle acceleration, i.e., classical second-order Fermi and shear acceleration, for understanding the multi-wavelength observations of the inner jets of M87. An analytical Fokker-Planck description is adopted to infer characteristic spectral indices and cutoff energies for these two mechanisms. We focus on electron synchrotron radiation as the dominant emission process. We find that the multi-wavelength observations of M87 can be satisfactorily accounted for in a framework, where the X-rays are produced at a larger distance from the core than the radio emission region. This provides further support to multi-zone, broadband emission modelling. We use our findings to also comment on the acceleration of cosmic rays entrained in the sheath.

## 1. INTRODUCTION

Relativistic jets seen in Active Galactic Nuclei (AGNs) are tightly collimated plasma outflows launched from the vicinity of their central supermassive black holes (SMBHs). Radio Very-Long-Baseline Interferometry (VLBI) observations have become an indispensable tool to investigate the detailed structure of these jets. In particular, in-depth studies of the relativistic jet in the radio galaxy M87 have provided new insights into its inner region (Asada & Nakamura 2012; Hada et al. 2013, 2016; Nakamura & Asada 2013; Kim et al. 2018; Walker et al. 2018; Event Horizon Telescope Collaboration et al. 2019; Park et al. 2019; Lu et al. 2023), revealing the limb-brightened structure and parabolic shape of the jet collimation and acceleration zone. Similar limb-brightened structures have also been detected in the jets of other low-luminosity AGNs, such as Cen A (Janssen et al. 2021), Mkn 501 (Piner et al. 2009), 3C84 (Giovannini et al. 2018) and 3C 273 (Bruni et al. 2021). Magnetohydrodynamic (MHD) jet models provide a well-developed framework to account for these structures (e.g., Mizuno 2022, for a review).

Relativistic AGN jets are known to emit non-thermal radiation by synchrotron and inverse Compton processes, from radio to X-rays up to  $\gamma$ -ray energies (e.g., Blandford et al. 2019). For the prominent radio galaxy M87, EHT MWL et al. (2021) have recently assembled a quasi-simultaneous multi-wavelength (MWL) spectral energy distribution (SED). Based on isotropic, leptonic single-zone emission models, they concluded that a structured jet such as a two-component, fast-spine and slow-sheath, jet may be needed to properly account for its broadband SED, similar to earlier expectations (Tavecchio & Ghisellini 2008). While in reality the situation might be more complex (e.g., Rieger & Aharonian 2012; Ait Benkhali et al. 2019; Lucchini et al. 2019), a spine-sheath jet topology provides an important generalization for particle acceleration and emission modelling (e.g., Rieger & Duffy 2004; Wang et al. 2021). Spine-sheath type jet structures are in fact naturally produced in general relativistic MHD simulations of magnetized accretion flow onto a rotating SMBH (McKinney 2006; Hardee et al. 2007; Porth et al. 2019; Chatterjee

et al. 2019). In the case of M87, significant structural patterns across its sub-parsec scale jet have been detected, validating the presence of both, slow ( $\sim 0.5c$ ) and fast ( $\sim 0.92c$ ) flow components (Mertens et al. 2016). On (sub-)parsec scales, recent studies of M87 have also reported quasi-periodic sideways motion of the inner structure based on long-term monitoring observations (Britzen et al. 2017; Walker et al. 2018; Ro et al. 2023). In addition, high dynamic range Very Long Baseline Array observations have revealed three helical threads inside the jet (Nikonov et al. 2023). It seems likely that these phenomena are related to the propagation of jet instabilities, such as Kelvin-Helmholtz (KHI) or current-driven kink ones, and/or caused by perturbed mass injection into the jet. They are indicative of a mildly turbulent nature in the sheath due to instabilities.

The non-thermal radiation observed from AGN jets provides clear evidence for the occurrence of particle acceleration such as facilitated by, e.g., diffusive shock and/or stochastic Fermi-type processes (e.g., Matthews et al. 2020). Shocks are suggested to be responsible for, e.g., the knotted structures in jets such as HST-1 in M87, the hot spots observed in giant radio lobes and polarization features in blazars (e.g., Blandford et al. 2019; Liodakis et al. 2022), while stochastic Fermi-type acceleration has been considered to account for the seemingly required hard particle spectra in TeV blazars (Lefa et al. 2011; Tavecchio et al. 2022), see also (Katarzyński et al. 2006), and to provide a promising explanatory framework for understanding the extended, high-energy emission in large-scale AGN jets (e.g., Wang et al. 2021; He et al. 2023).

In this paper, we focus on the MWL emission of the inner jet of M87 on scales below HST-1, where high-angular-resolution observations reveal continuous emission along its parsec-scale jet (e.g., EHT MWL et al. 2021). This would seem to require the operation of some *distributed in-situ* acceleration mechanism, and is more conveniently accommodated in a stochastic acceleration scenario than via localized shock acceleration. Alternatively, interaction with multiple shocks could be envisaged, potentially also resulting in spectral hardening of the accelerated particle distribution (e.g., Blandford & Königl 1979; Pope & Melrose 1994; Zech & Lemoine 2021). On the other hand, these shocks would require sufficiently low jet magnetization to make acceleration feasible (e.g., Crumley et al. 2019). Given that radio observations seemingly favor a structured jet model, we explore here the potential of stochastic Fermi-type particle acceleration as prototypical distributed mechanisms to understand the MWL observations of the inner jets in AGNs. In Section 2, we detail essential parts of the processes under consideration. In Section 3, we apply them to the inner jets of M87. Conclusions, along with a short discussion of cosmic ray acceleration, are presented in Section 4.

## 2. STOCHASTIC FERMI-TYPE PARTICLE ACCELERATION

### 2.1. Turbulent Fermi II and shear acceleration

In a spine-sheath type jet, as exemplified by M87, particles can be accelerated by scattering off moving, magnetic inhomogeneities embedded in the velocity-shearing jet flow, sampling both the velocity of MHD waves characterized by the Alfvén velocity  $\beta'_A$  and the velocity difference in the flow. In the following, we therefore explore particle acceleration through two types of stochastic Fermi-type processes: classical Fermi II and gradual shear acceleration (e.g., Rieger 2019; Lemoine 2019, for reviews). Since the scattering process (e.g., momentum-dependence) is most conveniently evaluated in the local (comoving) plasma frame, the particle transport is often described in a mixed-frame approach (e.g., Kirk et al. 1988; Webb et al. 2018). Hence, in the following, we mark expressions evaluated in the local frame by a prime. They can be related to the laboratory (lab.) frame ones by the corresponding Lorentz transformation with the jet bulk Lorentz factor ( $\Gamma_j$ ).

Stochastic particle acceleration essentially depends on the prevalent turbulence conditions. Following a phenomenological approach, we employ a (quasi-linear type) parameterization for the mean scattering time (see, e.g. Schlickeiser 2002)

$$\tau'_{sc} \approx \zeta^{-1} r'_L{}^{2-q} \lambda'_c{}^{q-1} c^{-1}, \quad (1)$$

where  $\zeta \equiv (\delta B')^2/B'^2 \leq 1$  is the ratio of turbulent magnetic energy to the total magnetic energy,  $\lambda'_c$  is the largest turbulence scale, and  $r'_L = \gamma' m_e c^2 / eB'$  is the Larmor radius of electrons with Lorentz factor  $\gamma'$ . The turbulence spectral index is usually in the range of  $1 \leq q \leq 2$ . Recent RMHD simulations of KHI-driven turbulence showed that the generated turbulence spectrum is largely consistent with a Kolmogorov-type behaviour ( $q = 5/3$ ) with  $\zeta \sim 10^{-3} - 10^{-2}$ , and that the largest turbulence scale is approximately given by the transverse jet scale ( $\lambda'_c \sim R$ ) in kinetic-energy-dominated jets with magnetisation  $B^2/8\pi\rho'c^2 \leq 0.2$ , where  $\rho'$  is the jet proper density and  $R$  is the jet radius (Wang et al. 2023). It should be noted that for magnetically dominated jets, the results for  $\zeta$  and  $q$  might be different, although details still remain to be explored.

Particle acceleration by stochastic Fermi-type processes can in principle be cast into a Fokker-Planck equation (e.g., Skilling 1975; Duffy & Blundell 2005), with momentum diffusion coefficient given by

$$D'(\gamma) \equiv \left\langle \frac{\Delta\gamma'^2}{\Delta t'} \right\rangle \approx A' \frac{\gamma'^2}{\tau'_{sc}}. \quad (2)$$

Given knowledge of the factor  $A'$ , the average energy change per scattering can be readily obtained by means of the Fokker-Planck relation  $\langle \frac{\Delta\gamma'}{\Delta t'} \rangle = \frac{\partial(\gamma'^2 D'(\gamma'))}{2\gamma'^2 \partial\gamma'}$ .

In Fermi II acceleration, particle energization is due to scattering off randomly moving MHD turbulence, thus the average energy gain is typically characterized by the Alfvén velocity, so that we have  $A'_{\text{Fermi-II}} \approx \beta_A'^2$  (e.g., Schlickeiser 2002; Stawarz & Petrosian 2008). In gradual shear acceleration, on the other hand, the turbulence is considered to be embedded in a velocity-shearing flow, so that the average energy gain is essentially related to the change in bulk flow velocity per scattering, i.e.,  $A'_{\text{shear}} \approx \frac{1}{15} \left( \Gamma_j^2(r) \frac{\partial\beta_j(r)c}{\partial r} \tau'_{sc} \right)^2$ , where  $\Gamma_j\beta_j c$  is the jet four velocity (e.g., Rieger & Duffy 2006; Liu et al. 2017; Webb et al. 2018).

The characteristic acceleration time scale is approximately given by  $\tau'_{\text{acc}} = \gamma' / \langle \Delta\gamma' / \Delta t' \rangle$ . For Fermi II acceleration (e.g., Stawarz & Petrosian 2008; Liu et al. 2017), this implies an acceleration time scale

$$\begin{aligned} \tau'_{\text{Fermi-II}} &= 2(2+q)^{-1} c^{3-2q} B'^{q-2} e^{q-2} m_e^{2-q} \gamma'^{2-q} \lambda_c'^{q-1} A'_{\text{Fermi-II}}^{-1} \zeta^{-1}, \\ &\approx 1.5 \times 10^{-4} R_{-2}^{2/3} \gamma'^{1/3} B'_{-1}{}^{-1/3} \beta_A'^{-2} \zeta_{-2}^{-1} \text{ yrs}, \end{aligned} \quad (3)$$

where  $R \equiv 10^{-2} R_{-2}$  pc,  $B' \equiv 0.1 B'_{-1}$  G, and  $\zeta \equiv 10^{-2} \zeta_{-2}$ . For quantitative evaluation, we have taken  $\lambda_c' \sim R$  and  $q = 5/3$  in the final step of this equation and subsequent relevant equations. For shear acceleration, the radial velocity profile of the jet becomes relevant. Following Eqs. (4), (7), and (11) in Wang et al. (2021), we define a parameter  $w$  to take this into account,

$$w = 4.5 \frac{\tau'_{\text{shear}}}{\tau'_{\text{esc}}} = \frac{10c^2}{\Gamma^4(r) R^2} \left( \frac{\partial u(r)}{\partial r} \right)^{-2}, \quad (4)$$

where the diffusive lateral escape time scale is

$$\tau'_{\text{esc}} = 1.5 (R/c)^2 \tau'_{sc}{}^{-1} = 6.0 B'_{-1}{}^{1/3} \zeta_{-2} R_{-2}^{4/3} \gamma'^{-1/3} \text{ yrs}. \quad (5)$$

This factor  $w$  has been obtained for different types of velocity shearing profiles (Rieger & Duffy 2019, 2022; Webb et al. 2019, 2023; Wang et al. 2023). The resultant mean shear acceleration time is

$$\begin{aligned} \tau'_{\text{shear}} &= 1.5 (6-q)^{-1} w B'^{2-q} e^{2-q} m_e^{q-2} \gamma'^{q-2} R^2 \lambda_c'^{1-q} \zeta, \\ &= 1.4 \eta R_{-2}^{4/3} B'_{-1}{}^{1/3} w \zeta_{-2} \gamma'^{-1/3} \text{ yrs}, \end{aligned} \quad (6)$$

where we have introduced a factor  $\eta \lesssim 1$  in order to accommodate different spatial dependencies (cf. Rieger & Duffy, in preparation). In particular, for highly relativistic flow speeds, regions of faster ( $\eta \ll 1$ ) acceleration are expected to show up in the resultant particle spectrum. Since we focus on mildly relativistic flows, we take here  $\eta = 1$  as a conservative estimate for the shear acceleration time.

In general, energetic electrons will also suffer from radiative losses and diffusive escape. The typical cooling time for synchrotron radiation is

$$\tau'_{\text{syn}} = 6\pi m_e c \sigma_T^{-1} \gamma'^{-1} B'^{-2} = 2.5 \times 10^3 \gamma'^{-1} B'_{-1}{}^{-2} \text{ yrs}, \quad (7)$$

where  $\sigma_T$  is the Thomson scattering cross-section. On the other hand, the dynamical time scale of the jet (as measured in the lab. frame) is

$$\tau_{\text{dyn}} = z / (\beta_j c) = 0.3 z_{-1} / \beta_j \text{ yrs}, \quad (8)$$

where  $z$  is the relevant jet length with  $z_{-1} \equiv z / 0.1$  pc. When the acceleration time is smaller than the dynamical time, the steady-state solution appears appropriate to study the particle spectrum. As we consider below an expanding jet with a collimation profile  $R \propto z^{k_1}$  with  $0 < k_1 < 1$ , particles will in principle also undergo adiabatic cooling. However, the corresponding cooling time scale is of the order  $\tau_{\text{ad}} \simeq R / \dot{R} = \tau_{\text{dyn}} / k_1$ , and typically less constraining than the dynamical time.

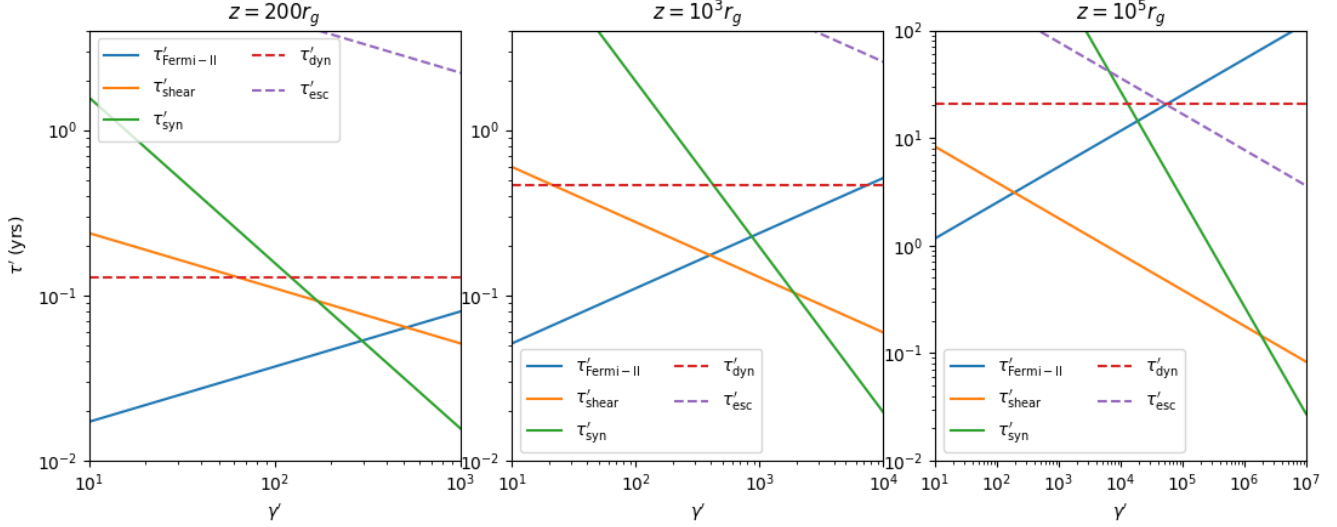


**Figure 1.** Illustration of the relevant timescales for electrons as seen in the comoving frame. For all three figures, we have fixed  $w = 0.1$ ,  $\beta'_A = 0.1$  and  $\zeta_{-2} = 1$ . From left to right, the timescales are for an M87 type jet at  $z = (200, 10^3, 10^5)r_g$  with parameters  $R_{-2} = (1.4, 3.9, 69)$ ,  $B'_{-1} = (12, 3.5, 0.1)$ , and  $\Gamma_j = (1.9, 2.4, 5.0)$ .

## 2.2. Resultant particle spectrum and cut-off energy

In turbulent shearing flows, Fermi II acceleration and shear acceleration are expected to operate simultaneously. In Fig. 1, we show the characteristic time scales in the co-moving frame ( $\tau' = \tau/\Gamma_j$ ) for three illustrative examples at different  $z$ . For these examples, typical values have been adopted as appropriate for the jet in M87 employing empirical jet profiles that largely follow the observations for jet radius (Asada & Nakamura 2012; Nakamura et al. 2018), Lorentz factor<sup>1</sup> (Park et al. 2019) and magnetic field (Ro et al. 2023),

$$R(z) = 1.67r_g(z/r_g)^{0.625}, \quad \Gamma_j(z) = 0.8(z/r_g)^{0.16}, \quad B'(z) \propto (\Gamma_j R)^{-1} = 80(z/r_g)^{-0.785} \text{ G}. \quad (9)$$

Inspection of Fig. 1 reveals that without particle acceleration electrons would cool down significantly due to synchrotron radiation within the dynamical time for the chosen parameters of M87, as indicated by the intersection point of the solid green line and the dashed red line. This suggests that an *in-situ* acceleration mechanism is required to account for the observed, extended radio emission along the inner jet. In addition, since for both acceleration mechanisms considered here, the dynamical time is in general much longer, a steady-state solution approach to the particle spectra is feasible. Fig. 1 also indicates that for the jet in M87, Fermi II acceleration is likely to dominate the acceleration processes close to the black hole (e.g., at  $z \lesssim 200r_g$ ), while shear acceleration overtakes towards higher energies at larger distances (e.g., at  $z \gtrsim 10^3r_g$ ). The reason is that shear acceleration becomes more efficient at higher energies. As the magnetic field decreases with distance  $z$  for the M87 jet, the synchrotron cooling effect is reduced along  $z$ . This allows electrons to be accelerated to higher energies, facilitating shear acceleration.

The characteristic cutoff energy is limited by the balance between acceleration and cooling. For the Fermi II acceleration, the synchrotron-limited cutoff electron energy and corresponding synchrotron frequency are given by

$$\begin{aligned} \gamma'_{\text{cut, Fermi-II}} &= [1.125(2+q)A'_{\text{Fermi-II}}B^{-q}e^{-2-q}m_e^{1+q}\zeta^{2+2q}\chi_c^{1-q}\zeta]^{1/(3-q)}, \\ &= 2.6 \times 10^5 \beta_A'^{3/2} \zeta_{-2}^{3/4} B_{-1}'^{-5/4} R_{-2}^{-1/2}, \end{aligned} \quad (10)$$

$$\begin{aligned} \nu'_{\text{cut, Fermi-II}} &= 3\gamma_{\text{cut, Fermi-II}}'^2 eB/(4\pi m_e c), \\ &= 2.9 \times 10^7 \beta_A'^3 \zeta_{-2}^{3/2} B_{-1}'^{-3/2} R_{-2}^{-1} \text{ GHz}. \end{aligned} \quad (11)$$

The cutoff Lorentz factor and corresponding frequency for the Fermi II acceleration depend mainly on the Alfvén velocity, the turbulent energy density ratio ( $\zeta$ ), the jet magnetic field and radius. The observed frequency can be

<sup>1</sup> We choose a slightly higher coefficient for the Lorentz factor profile to guarantee  $\Gamma \geq 1$  for a large range of  $z$ .

obtained by a Doppler transformation  $\nu_{\text{obs}} = \delta_{\text{D}} \nu'$ , where  $\delta_{\text{D}} = [\Gamma_{\text{j}}(1 - \beta_{\text{j}} \cos i)]^{-1}$  denotes the Doppler factor, with  $i$  being the jet axis angle to the line of sight.

As shown in Fig. 1, the escape time is usually much larger than the acceleration time, so that we can assume an inefficient escape. For  $q = 5/3$ , an analytical solution of the Fokker-Planck equation for the Fermi II acceleration is not readily available, but a cutoff power-law (CPL) spectrum might serve as a good approximation (e.g., Lacombe 1979; Stawarz & Petrosian 2008),

$$N(\gamma') \propto \gamma'^{-p} \exp[-(\frac{\gamma'}{\gamma'_{\text{cut,Fermi-II}}})^{3-q}]. \quad (12)$$

For  $\gamma' \ll \gamma'_{\text{cut,Fermi-II}}$ , synchrotron cooling is insignificant and the spectrum behaves as a power law with an index  $p_{\text{Fermi-II}} = q - 1 = 2/3$  (e.g., Lacombe 1979; Stawarz & Petrosian 2008). Towards higher energies ( $\gamma' \lesssim \gamma'_{\text{cut,Fermi-II}}$ ), when electron synchrotron cooling becomes important, the spectral shape often has a pile-up, approximately described by a Maxwellian-type particle distribution  $N(\gamma') \propto \gamma'^2 \exp[-(\gamma'/\gamma'_{\text{cut,Fermi-II}})^{3-q}]$  (cf., Schlickeiser 1985; Becker et al. 2006; Stawarz & Petrosian 2008; Lefa et al. 2011), see also (Lemoine & Malkov 2020) for discussion. Here we adopt only the CPL spectrum and ignore pile-up effects. We note that if particle acceleration would proceed very efficiently, turbulence damping may occur, self-regulating the process and introducing some spectral steepening.

The characteristic cutoff electron energy and the corresponding cutoff synchrotron radiation frequency for shear acceleration are given by

$$\begin{aligned} \gamma'_{\text{cut,sh}} &= [2(18 - 3q)^{-1} B^{4-q} e^{6-q} m_e^{q-5} c^{2q-10} w R^2 \lambda_c^{1-q} \zeta]^{1/(1-q)}, \\ &= 7.5 \times 10^4 B'_{-1}{}^{-7/2} R_{-2}^{-2} \zeta_{-2}^{-3/2} w^{-3/2}, \end{aligned} \quad (13)$$

$$\begin{aligned} \nu'_{\text{cut,sh}} &= 3\gamma'_{\text{cut,sh}}{}^2 eB / (4\pi m_e c), \\ &= 2.4 \times 10^6 B'_{-1}{}^{-6} R_{-2}^{-4} w^{-3} \zeta_{-2}^{-3} \text{ GHz}. \end{aligned} \quad (14)$$

While in relativistic flows higher electron Lorentz factors can occur, we take Eq. (13) as conservative reference value here. It can be seen that the cutoff Lorentz factor and corresponding synchrotron frequency for shear acceleration have a strong dependence on the magnetic field, jet radius, the radial velocity profile parameter ( $w$ ), and the turbulent energy density ratio ( $\zeta$ ).

As in a leaky-box model approach, the particle escape time has the same scaling with  $\gamma'$  as the shear acceleration timescale, this needs to be suitably taken into account for evaluating the spectral index. In the steady state, the exact solution of the Fokker-Planck equation for shear acceleration is given by (Wang et al. 2021),

$$n(\gamma') \propto \gamma'^{s-} F_{-}(\gamma', q) + C \gamma'^{s+} F_{+}(\gamma', q), \quad (15)$$

$$s_{\pm} = \frac{q-1}{2} \pm \sqrt{\frac{(5-q)^2}{4} + w}, \quad (16)$$

$$F_{\pm}(\gamma', q) = {}_1F_1 \left[ \frac{2+s_{\pm}}{q-1}, \frac{2s_{\pm}}{q-1}; -\frac{6-q}{q-1} \left( \frac{\gamma'}{\gamma'_{\text{cut,sh}}} \right)^{q-1} \right], \quad (17)$$

where  ${}_1F_1$  is Kummer's confluent hypergeometric function (e.g., Abramowitz & Stegun 1972), and the integration constant  $C$  is determined by the condition  $n \rightarrow 0$  for  $\gamma \rightarrow \infty$ . For  $\gamma' \ll \gamma'_{\text{cut,sh}}$ , the particle spectrum behaves as a power law ( $n(\gamma') \propto \gamma'^{-p_{\text{shear}}}$ ) with index  $p_{\text{shear}} = -s_{-} = \sqrt{w + 25/9} - 1/3$  (Rieger & Duffy 2019; Wang et al. 2021; Rieger & Duffy 2022), where we have used  $q = 5/3$ . Near the cutoff, pile-up due to synchrotron cooling can occur. For a highly relativistic spine-sheath jet ( $w \rightarrow 0$ ), acceleration will be much more efficient than escape, leading to a hard particle spectrum with an index approaching  $p_{\text{shear}} = 4/3$  (Webb et al. 2018; Rieger & Duffy 2019). Synchrotron cooling, on the other hand, will introduce an exponential-like cutoff at high energies (Wang et al. 2021).

The transition energy from Fermi II acceleration to shear acceleration can be obtained by solving  $\tau'_{\text{shear}} = \tau'_{\text{Fermi-II}}$ , which gives

$$\gamma'_t = 9.2 \times 10^5 B'_{-1} R_{-2} \beta_A^3 w^{3/2} \zeta_{-2}^3. \quad (18)$$

Accordingly, the transition energy strongly depends on the considered shear coefficient  $w$ , the Alfvén velocity, and the turbulence energy ratio. The population of electrons energized by shear acceleration starts to emerge when  $\gamma'_{\text{cut,sh}} \geq \gamma'_t$ , implying  $B'_{-1} \leq 0.57 R_{-2}^{-2/3} w^{-2/3} \beta_A^{-2/3} \zeta_{-2}^{-1}$ .

### 2.3. Particle acceleration along the jet

Since the jet parameters evolve over jet length ( $z$ ), one can also evaluate the dependence of particle acceleration on  $z$ . As above, we assume  $R \propto z^{k_1}$  and  $\Gamma_j \propto z^{k_2}$  with  $k_2 > 0$ , so that  $B' \propto (R\Gamma_j)^{-1} \propto z^{-(k_1+k_2)}$  from the conservation of magnetic flux. We note that theoretically,  $k_1$  and  $k_2$  can be related. For a highly magnetised cold jet, for example, there are regimes depending on the external gas pressure profile with  $k_1 = k_2$  or  $k_2 = 2k_1 - 1$  (Lyubarsky 2009). For our discussions below, we keep both  $k_1$  and  $k_2$  as independent parameters and assume that  $w$  and  $\zeta$  is uniform along the jet. For electrons, the characteristic particle Lorentz factor in the comoving frame by shear acceleration is given by Eq. (13). If the sheath would follow the jet scaling, the shear cutoff Lorentz factor would scale as  $\gamma'_{\text{cut,sh}} \propto z^{(3k_1+7k_2)/2}$ . For the Fermi II acceleration, we have  $\gamma'_{\text{cut,Fermi-II}} \propto z^{(3k_1+5k_2)/4}$  from Eq. (10) assuming  $\beta'_A$  to also remain constant along the jet. The cutoff synchrotron frequencies in the comoving frame are then  $\nu'_{\text{cut,sh}} \propto z^{2(k_1+3k_2)}$ , and  $\nu'_{\text{cut,Fermi-II}} \propto z^{(k_1+3k_2)/2}$ . Accordingly, for both mechanisms, the cutoff electron energy and synchrotron photon energy becomes larger at larger  $z$ . We note that in principle  $\beta'_A$  may also grow with  $z$  following  $\beta'_A \propto B'/\sqrt{\rho'} \propto \sqrt{\beta_j}$ , where  $\rho' \propto \beta_j^{-1}(\Gamma_j R)^{-2}$  has been assumed, making the Fermi II slightly more efficient at higher  $z$ .

## 3. APPLICATIONS TO RESOLVED JETS

### 3.1. General discussion of the spine-sheath structure

As shown above, electrons accelerated through shear or Fermi II acceleration processes can in principle produce synchrotron emission, and thus potentially account for some of the inner jet emission. This seems particularly interesting in the context of recent radio observations which have allowed one to resolve the innermost jet regions in M87 and Cen A in unprecedented detail. In particular, an edge-brightened morphology extending up to a few thousands of gravitational radii ( $r_g = GM_{\text{BH}}/c^2$ ) has been observed in both sources (e.g. Kim et al. 2018; Janssen et al. 2021). This could be a natural consequence of a spine-sheath jet. As argued by Janssen et al. (2021), assuming identical intrinsic emissivities for both, the fast spine and the slow sheath, the brightness asymmetry seen in Cen A could in principle be explained by the beaming effect if the spine velocity  $\beta_{j,\text{sp}} > \cos i_{\text{CenA}}$ , where  $i$  is the inclination angle. On the other hand, if the sheath would be symmetric around the spine, edge-brightening could be caused by path length differences and/or the presence of a helical magnetic field component. Fermi-type particle acceleration may further add to this. In particular, shear acceleration will mainly take place in the sheath region where a significant velocity gradient exists. Moreover, the sheath is typically prone to KHI as indicated by the quasi-periodic sideways motions of the jet (Walker et al. 2018), and since there is no evidence of strong instability in the spine, the sheath could be more turbulent, facilitating particle acceleration. One may thus anticipate that particle acceleration by shear and the Fermi II processes become more efficient in the sheath. Since we do not consider the sheath on those scales to be highly magnetized, particle acceleration by reconnection is not included in the modeling below. We note, however, that in the case of a highly magnetized ( $\sigma \gg 1$ ) sheath, reconnection has been shown to facilitate electron acceleration to  $\gamma_e \sim \mathcal{O}(10)$  (e.g., Sironi et al. 2021), potentially providing pre-accelerated seed particles for further shear acceleration.

### 3.2. MWL modelling of the inner jet of M87

In the following, we take the inner jet of M87 as an example, utilizing data from an extensive MWL observation campaign performed in 2017 (see EHT MWL et al. 2021, and references therein). Since observations at different wavelengths have different angular resolutions (cf. their table A8), we include radio observations (resolution  $\sim 0.1 - 1$  mas) and keep X-ray observations (resolution  $0.8''$ ) from Chandra and NuSTAR, where the dominant component is the inner jet (EHT MWL et al. 2021). Swift X-ray data and gamma-ray data are excluded as their origin is uncertain due to their angular resolutions ( $> 30''$ ). For studying the emission from the inner jet, we concentrate on radio data from observations with an angular resolution of  $(130 - 1300)r_g$  (EHT MWL et al. 2021) shown as blue data points in Fig. 2. The radio data of the core with angular resolution  $(15.5 - 52)r_g$  are shown as orange data points in Fig. 2. The SMBH mass of M87 is  $M_{\text{BH}} \simeq 6.5 \times 10^9 M_{\odot}$  (Gebhardt et al. 2011; Event Horizon Telescope Collaboration et al. 2019), which corresponds to a gravitational radius  $r_g \simeq 9.6 \times 10^{14}$  cm. The radio to X-ray data from a larger region associated with angular resolutions of  $(1.3 \times 10^4 - 3 \times 10^5)r_g$  are shown by cyan data points.

The detected radio SED is mainly from the jet within a projected size of  $650r_g$  (half of the angular resolution) or a de-projected distance  $z = 650r_g / \sin i_{\text{M87}} = 2.2 \times 10^3 r_g$ , where we have taken an inclination  $i_{\text{M87}} = 17^\circ$  (Event Horizon Telescope Collaboration et al. 2019; EHT MWL et al. 2021). However, at lower frequencies ( $\lesssim 86$  GHz) the core is expected to be optically thick due to synchrotron self-absorption (EHT MWL et al. 2021). Thus we focus on the

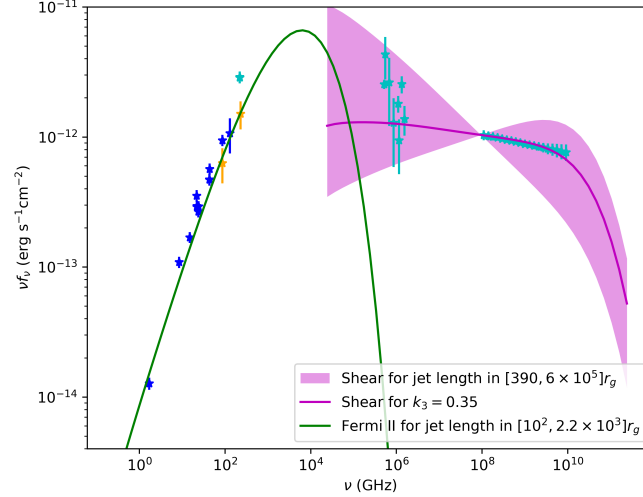


**Figure 2.** Exemplary reproduction of the SED of the inner jet of M87. The MWL data are shown with asterisk points and the characteristic SEDs of electron synchrotron radiation are shown with lines. The orange, blue, and cyan data points are taken from a region of de-projected distances  $z < 26.5 - 89r_g$ ,  $z < 222 - 2.2 \times 10^3 r_g$  and  $z < 4.4 \times 10^5 - 10^6 r_g$ , respectively. The radio SED is modelled by Fermi II acceleration (green line) from the jet within  $[10^2, 2.2 \times 10^3] r_g$ . The optical to X-ray SED is modelled with shear acceleration from the jet within  $[390, 6 \times 10^5] r_g$  (magenta line and shaded area). The theoretical SEDs are normalized to match the first X-ray data point.

region within  $[10^2, 2.2 \times 10^3] r_g$ . With jet axial profiles following Eq. (9), and adopting  $\lambda'_c \sim R$ ,  $\zeta_{-2} = 1$  and  $q = 5/3$  for the turbulence,  $\beta'_A = 0.1$  for Fermi II acceleration and  $w = 0.1$  for shear acceleration, the synchrotron emission at the scale  $[10^2, 2.2 \times 10^3] r_g$  is mainly contributed by Fermi II acceleration. Shear-accelerated electrons start to appear at energies  $\gamma' \gtrsim 450$  on scales of  $z \gtrsim 400 r_g$ , see Eq. (18) and Fig. 1. An earlier onset is in principle possible for smaller  $\beta'_A$ ,  $\zeta$  or  $w$ . In general, the cutoff synchrotron frequency for shear acceleration grows much faster than for the Fermi II with  $\nu'_{\text{cut,sh}}(z) \propto B(z)^{-6} R(z)^{-4} \propto z^{2.21}$  and  $\nu'_{\text{cut,Fermi-II}} \propto B(z)^{-3/2} R(z)^{-1} \propto z^{0.55}$ , respectively. Thus shear acceleration will dominate the optical to X-ray emission. To produce X-ray photons up to tens of keV, we require a jet length  $z \sim 6 \times 10^5 r_g$  for the adopted profiles in Eq. (9) and the assumed parameters  $w = 0.1$  and  $\zeta_{-2} = 1$ , which is approximately within the distance of the HST-1 knot. Hence, in the following, we also take into account the contribution by shear-accelerated electrons within  $[390, 6 \times 10^5] r_g$ . Note that the cutoff synchrotron frequency depends also on  $w$  and  $\zeta$  with  $\nu'_{\text{cut,sh}} \propto (w * \zeta)^{-3}$ , so that a smaller value of  $w * \zeta$  can accommodate a smaller jet length  $z$ .

The synchrotron radiation at a certain jet length  $z$  is given by

$$f_\nu(z) dz = \delta_D^3(z) S(z) dz \int_{\gamma'_{\min}}^{+\infty} n'(\gamma', z) F_{\text{syn}}(\gamma', \nu') d\gamma', \quad (19)$$

where  $F_{\text{syn}}$  is the synchrotron emissivity for electrons with energy  $\gamma'$ . We chose  $\gamma'_{\min} = 5$  as the minimum Lorentz factor for Fermi II acceleration and  $\gamma'_{\min} = \gamma'_t$  (Eq. 18) for shear acceleration. The emitting area ( $S \leq \pi R^2$ ) and differential electron number density ( $n'$ ) relate to the acceleration mechanism. The particle spectral shape follows Eq. (12) with  $p_{\text{Fermi-II}} = 2/3$  for Fermi II acceleration, or Eqs. (15-17) for shear acceleration with a spectral index  $p_{\text{shear}} \approx 1.36$  by taking  $w = 0.1$ . The latter constraint would mimic a fast and sharp velocity profile (Rieger & Duffy 2019, 2022; Wang et al. 2023).

The total emission along the jet is obtained by

$$f_\nu = \int_{z_{\min}}^{z_{\max}} f_\nu(z) dz. \quad (20)$$

For Fermi II acceleration with  $(z_{\min}, z_{\max}) = (10^2, 2.2 \times 10^3) r_g$ , we assume that the emitting area grows with jet radius,  $S(z) \propto \pi R(z)^2$ , and that the number density scales with the jet plasma density, namely  $n'(z) \propto \rho'(z)$ . For a cold jet, the jet kinetic luminosity is  $L_j = \pi R^2 \beta_j c \Gamma_j (\Gamma_j - 1) \rho' c^2$ , so that we have  $n'(z) \propto \rho'(z) \propto 1/[R^2 \beta_j(z) \Gamma_j(z) (\Gamma_j(z) - 1)]$ . The resultant SED is shown with a green line in Fig. 2. For shear acceleration with  $(z_{\min}, z_{\max}) = (390, 6 \times 10^5) r_g$ , the situation is more complex. As the jet spine velocity grows with  $z$ , the Doppler factor achieves its maximum

$\delta_{D,\max} = 1/\sin i_{M87}$  at  $\beta_j = \cos i_{M87}$ , which occurs at  $z_D = 8.8 \times 10^3 r_g$  for the velocity profile of Eq. (9). At  $z > z_D$ , the Doppler factor for the spine decreases with  $z$  as  $\beta_j > \cos i_{M87}$ . However, the Doppler factor remains  $\delta_{D,\text{sh}} = \delta_{D,\max}$  in the sheath region with  $\beta_{j,\text{sh}} = \cos i_{M87}$ . Since the SED depends on the Doppler factor with  $\nu f_\nu \propto \delta_D^4$ , we mainly trace the region of  $\beta_{j,\text{sh}} \sim \cos i_{M87}$  for the synchrotron radiation from  $z > z_D$  and assume the dominant emitting area to be roughly constant,  $S(z) \propto z^0$ . Similar to the above, we consider a scaling  $n'(z) \propto \rho'(z)$  for the particle number density. The corresponding total energy density is  $E'_e \propto \int_{\gamma'_t}^{\gamma'_{\text{cut,sh}}} n'(\gamma') \gamma' d\gamma' \propto \gamma'^{0.64}_{\text{cut,sh}}$  for a spectral index  $p_{\text{shear}} \approx 1.36$ . The cutoff electron Lorentz factor for shear acceleration obeys  $\gamma'_{\text{cut,sh}} \propto z^{1.5}$  and grows to  $\sim 10^6$  at  $z = 10^5 r_g$  (Fig. 1). Hence, in this case, the total energy of shear-accelerated electrons would grow as  $E'_e \propto z^{0.95}$ , implying an increasing energy deposition rate from turbulent energy into shear-accelerated electrons. However, once the energy density in non-thermal particles sufficiently exceeds the turbulent magnetic energy density, back-reaction sets in with the turbulence becoming damped and acceleration suppressed (e.g., Lemoine et al. 2023). We thus treat  $n'(z) \propto \rho'(z)$  as an upper limit for shear acceleration, and allow for some extra dependence on  $z$  to account for a changing energy deposition rate, i.e.  $n'(z) \propto z^{k_3} \rho'(z)$ . A lower limit is obtained for a constant energy deposition rate ( $E'_e z^{k_3} \propto z^0$ ) with  $k_3 = -0.95$ . The resultant SED for shear acceleration is shown in magenta color in Fig. 2, where the shaded area covers a range  $[390, 6 \times 10^5] r_g$  and  $-0.95 \lesssim k_3 \lesssim 0$ , and the solid line assumes  $k_3 = -0.35$ . Our modelling indicates that the observed SED can be explained with a moderately changing energy deposition rate with  $k_3 = -0.35$ .

#### 4. CONCLUSION AND DISCUSSION

The particle acceleration mechanism in the inner jets of AGNs resolved by VLBI observations is still unclear. In this work, we have explored the potential role of shear and classical second-order Fermi acceleration in mildly relativistic jet flows such as expected in M87. The application of these stochastic acceleration mechanisms makes it possible to account for extended radio features, and to infer characteristic cutoff particle energies and particle spectral indices. In this scenario, the limb-brightening structure might not only be related to different path lengths and magnetic fields, but also to different turbulence structures between the spine and the sheath. In general, the maximum synchrotron frequency depends strongly on the jet magnetic field, the radial velocity profile parameter ( $w$ ), and the turbulent energy density ratio ( $\zeta$ ) for shear acceleration (Eq. 14). As the magnetic field decreases over jet length ( $z$ ), the high-energy emission, such as X-rays, will be dominated by high- $z$  regions. The spectral index is determined by both the local particle distribution (Eqs. 12 and 15) and its evolution over jet length ( $n'(z) \propto z^{k_3} \rho'(z)$ ), where  $k_3$  relates to the interaction between non-thermal particles and turbulence. These jet dynamical details could be probed by future numerical simulations.

By adopting a simple model for electron synchrotron radiation in M87 on scales  $z \geq 100 r_g$ , we have shown that stochastic Fermi-type particle acceleration can qualitatively reproduce the MWL SED of its inner jet. While the radio band can be successfully accounted for by second-order Fermi acceleration, the optical to X-ray band can be modelled by synchrotron radiation from shear-accelerated electrons energized at larger distances,  $z \in [390, 6 \times 10^5] r_g$ . Particle acceleration at shocks could yield more localized structures, such as the HST-1 knot at  $\sim 10^6 r_g$  (e.g. Asada & Nakamura 2012; Blandford et al. 2019), while reconnection might facilitate electron seed injection into Fermi-type particle acceleration especially below several hundreds  $r_g$  (e.g., Sironi et al. 2021; Cruz-Orsorio et al. 2022; Yang et al. 2024). Although the broadband emission in the considered framework arises in an extended region, variability could be triggered by, e.g., jet instabilities and/or non-uniform accretion that enhance the number of non-thermal particles in certain jet distances, leading to flares in certain energy bands (e.g., Mizuno et al. 2012; Singh et al. 2016).

We note that as the jet propagates, material from the ambient medium such as from a Blandford-Payne driven jet (Blandford & Payne 1982) from the disk is likely to get entrained in the sheath region. Thus the sheath may contain a significant fraction of baryonic matter. These particles might also undergo acceleration, as required for hadronic radiation models and neutrino productions. Focusing on protons, our results suggest that shear acceleration is more efficient than Fermi II acceleration ( $\tau'_{\text{shear}} < \tau'_{\text{Fermi-II}}$ ) for  $\gamma' > 5 \times 10^2 B'_{-1} R_{-2} \beta_A^3 w^{3/2} \zeta_{-2}^3$ . Since synchrotron cooling for protons is usually negligible, the limiting factor mainly comes from the dynamical time. Requiring  $\tau'_{\text{sc}} \lesssim \tau'_{\text{dyn}}$ , yields a constraint in the comoving frame of  $\gamma'_p \lesssim 10^6 B'_{-1} \zeta_{-2}^2 z_{-1}^3 \beta_j^{-3} \Gamma_j^{-3} R_{-2}^{-2}$ , which increases with  $z$ . Therefore, protons might be continuously accelerated along the jet as long as the Hillas limit  $\gamma'_{p,\text{Hillas}} \lesssim 10^9 \beta_j B'_{-1} R_{-2}$  is satisfied.



## ACKNOWLEDGMENTS

We are grateful to the referee for constructive suggestions and S. Markoff and B. Reville for discussions. JSW acknowledges support from the Alexander von Humboldt Foundation, and FMR support by the DFG under RI 1187/8-1. YM is supported by the National Key R & D Program of China (grant no. 2023YFE0101200), the National Natural Science Foundation of China (grant no. 12273022), and the Science and Technology Commission of Shanghai Municipality orientation program of basic research for international scientists (grant no. 22JC1410600).

*Software:* Astropy (Astropy Collaboration et al. 2022); Mathematica (Wolfram Research 2023); Matplotlib (Hunter 2007); Naima (Zabalza 2015)

## REFERENCES

- Abramowitz, M., & Stegun, I. A. 1972, Handbook of Mathematical Functions
- Ait Benkhali, F., Chakraborty, N., & Rieger, F. M. 2019, A&A, 623, A2, doi: [10.1051/0004-6361/201732334](https://doi.org/10.1051/0004-6361/201732334)
- Asada, K., & Nakamura, M. 2012, ApJL, 745, L28, doi: [10.1088/2041-8205/745/2/L28](https://doi.org/10.1088/2041-8205/745/2/L28)
- Astropy Collaboration, Price-Whelan, A. M., Lim, P. L., et al. 2022, ApJ, 935, 167, doi: [10.3847/1538-4357/ac7c74](https://doi.org/10.3847/1538-4357/ac7c74)
- Becker, P. A., Le, T., & Dermer, C. D. 2006, ApJ, 647, 539, doi: [10.1086/505319](https://doi.org/10.1086/505319)
- Blandford, R., Meier, D., & Readhead, A. 2019, ARA&A, 57, 467, doi: [10.1146/annurev-astro-081817-051948](https://doi.org/10.1146/annurev-astro-081817-051948)
- Blandford, R. D., & Königl, A. 1979, ApJ, 232, 34, doi: [10.1086/157262](https://doi.org/10.1086/157262)
- Blandford, R. D., & Payne, D. G. 1982, MNRAS, 199, 883, doi: [10.1093/mnras/199.4.883](https://doi.org/10.1093/mnras/199.4.883)
- Britzen, S., Fendt, C., Eckart, A., & Karas, V. 2017, A&A, 601, A52, doi: [10.1051/0004-6361/201629469](https://doi.org/10.1051/0004-6361/201629469)
- Bruni, G., Gómez, J. L., Vega-García, L., et al. 2021, A&A, 654, A27, doi: [10.1051/0004-6361/202039423](https://doi.org/10.1051/0004-6361/202039423)
- Chatterjee, K., Liska, M., Tchekhovskoy, A., & Markoff, S. B. 2019, MNRAS, 490, 2200, doi: [10.1093/mnras/stz2626](https://doi.org/10.1093/mnras/stz2626)
- Crumley, P., Caprioli, D., Markoff, S., & Spitkovsky, A. 2019, MNRAS, 485, 5105, doi: [10.1093/mnras/stz232](https://doi.org/10.1093/mnras/stz232)
- Cruz-Osorio, A., Fromm, C. M., Mizuno, Y., et al. 2022, Nature Astronomy, 6, 103, doi: [10.1038/s41550-021-01506-w](https://doi.org/10.1038/s41550-021-01506-w)
- Duffy, P., & Blundell, K. M. 2005, Plasma Physics and Controlled Fusion, 47, B667, doi: [10.1088/0741-3335/47/12B/S49](https://doi.org/10.1088/0741-3335/47/12B/S49)
- EHT MWL, Algaba, J. C., Anczarski, J., et al. 2021, ApJL, 911, L11, doi: [10.3847/2041-8213/abef71](https://doi.org/10.3847/2041-8213/abef71)
- Event Horizon Telescope Collaboration, Akiyama, K., Alberdi, A., et al. 2019, ApJL, 875, L1, doi: [10.3847/2041-8213/ab0ec7](https://doi.org/10.3847/2041-8213/ab0ec7)
- Gebhardt, K., Adams, J., Richstone, D., et al. 2011, ApJ, 729, 119, doi: [10.1088/0004-637X/729/2/119](https://doi.org/10.1088/0004-637X/729/2/119)
- Giovannini, G., Savolainen, T., Orienti, M., et al. 2018, Nature Astronomy, 2, 472, doi: [10.1038/s41550-018-0431-2](https://doi.org/10.1038/s41550-018-0431-2)
- Hada, K., Kino, M., Doi, A., et al. 2013, ApJ, 775, 70, doi: [10.1088/0004-637X/775/1/70](https://doi.org/10.1088/0004-637X/775/1/70)
- . 2016, ApJ, 817, 131, doi: [10.3847/0004-637X/817/2/131](https://doi.org/10.3847/0004-637X/817/2/131)
- Hardee, P., Mizuno, Y., & Nishikawa, K.-I. 2007, Ap&SS, 311, 281, doi: [10.1007/s10509-007-9529-1](https://doi.org/10.1007/s10509-007-9529-1)
- He, J.-C., Sun, X.-N., Wang, J.-S., et al. 2023, MNRAS, 525, 5298, doi: [10.1093/mnras/stad2542](https://doi.org/10.1093/mnras/stad2542)
- Hunter, J. D. 2007, Computing in Science & Engineering, 9, 90, doi: [10.1109/MCSE.2007.55](https://doi.org/10.1109/MCSE.2007.55)
- Janssen, M., Falcke, H., Kadler, M., et al. 2021, Nature Astronomy, 5, 1017, doi: [10.1038/s41550-021-01417-w](https://doi.org/10.1038/s41550-021-01417-w)
- Katarzyński, K., Ghisellini, G., Mastichiadis, A., Tavecchio, F., & Maraschi, L. 2006, A&A, 453, 47, doi: [10.1051/0004-6361:20054176](https://doi.org/10.1051/0004-6361:20054176)
- Kim, J. Y., Krichbaum, T. P., Lu, R. S., et al. 2018, A&A, 616, A188, doi: [10.1051/0004-6361/201832921](https://doi.org/10.1051/0004-6361/201832921)
- Kirk, J. G., Schlickeiser, R., & Schneider, P. 1988, ApJ, 328, 269, doi: [10.1086/166290](https://doi.org/10.1086/166290)
- Lacombe, C. 1979, A&A, 71, 169
- Lefa, E., Rieger, F. M., & Aharonian, F. 2011, ApJ, 740, 64, doi: [10.1088/0004-637X/740/2/64](https://doi.org/10.1088/0004-637X/740/2/64)
- Lemoine, M. 2019, PhRvD, 99, 083006, doi: [10.1103/PhysRevD.99.083006](https://doi.org/10.1103/PhysRevD.99.083006)
- Lemoine, M., & Malkov, M. A. 2020, MNRAS, 499, 4972, doi: [10.1093/mnras/staa3131](https://doi.org/10.1093/mnras/staa3131)
- Lemoine, M., Murase, K., & Rieger, F. 2023, arXiv e-prints, arXiv:2312.04443, doi: [10.48550/arXiv.2312.04443](https://doi.org/10.48550/arXiv.2312.04443)
- Liodakis, I., Marscher, A. P., Agudo, I., et al. 2022, Nature, 611, 677, doi: [10.1038/s41586-022-05338-0](https://doi.org/10.1038/s41586-022-05338-0)
- Liu, R.-Y., Rieger, F. M., & Aharonian, F. A. 2017, ApJ, 842, 39, doi: [10.3847/1538-4357/aa7410](https://doi.org/10.3847/1538-4357/aa7410)

- Lu, R.-S., Asada, K., Krichbaum, T. P., et al. 2023, *Nature*, 616, 686, doi: [10.1038/s41586-023-05843-w](https://doi.org/10.1038/s41586-023-05843-w)
- Lucchini, M., Krauß, F., & Markoff, S. 2019, *MNRAS*, 489, 1633, doi: [10.1093/mnras/stz2125](https://doi.org/10.1093/mnras/stz2125)
- Lyubarsky, Y. 2009, *ApJ*, 698, 1570, doi: [10.1088/0004-637X/698/2/1570](https://doi.org/10.1088/0004-637X/698/2/1570)
- Matthews, J. H., Bell, A. R., & Blundell, K. M. 2020, *NewAR*, 89, 101543, doi: [10.1016/j.newar.2020.101543](https://doi.org/10.1016/j.newar.2020.101543)
- McKinney, J. C. 2006, *MNRAS*, 368, 1561, doi: [10.1111/j.1365-2966.2006.10256.x](https://doi.org/10.1111/j.1365-2966.2006.10256.x)
- Mertens, F., Lobanov, A. P., Walker, R. C., & Hardee, P. E. 2016, *A&A*, 595, A54, doi: [10.1051/0004-6361/201628829](https://doi.org/10.1051/0004-6361/201628829)
- Mizuno, Y. 2022, *Universe*, 8, 85, doi: [10.3390/universe8020085](https://doi.org/10.3390/universe8020085)
- Mizuno, Y., Lyubarsky, Y., Nishikawa, K.-I., & Hardee, P. E. 2012, *ApJ*, 757, 16, doi: [10.1088/0004-637X/757/1/16](https://doi.org/10.1088/0004-637X/757/1/16)
- Nakamura, M., & Asada, K. 2013, *ApJ*, 775, 118, doi: [10.1088/0004-637X/775/2/118](https://doi.org/10.1088/0004-637X/775/2/118)
- Nakamura, M., Asada, K., Hada, K., et al. 2018, *ApJ*, 868, 146, doi: [10.3847/1538-4357/aaeb2d](https://doi.org/10.3847/1538-4357/aaeb2d)
- Nikonov, A. S., Kovalev, Y. Y., Kravchenko, E. V., Pashchenko, I. N., & Lobanov, A. P. 2023, arXiv e-prints, arXiv:2307.11660, doi: [10.48550/arXiv.2307.11660](https://doi.org/10.48550/arXiv.2307.11660)
- Park, J., Hada, K., Kino, M., et al. 2019, *ApJ*, 887, 147, doi: [10.3847/1538-4357/ab5584](https://doi.org/10.3847/1538-4357/ab5584)
- Piner, B. G., Pant, N., Edwards, P. G., & Wiik, K. 2009, *ApJL*, 690, L31, doi: [10.1088/0004-637X/690/1/L31](https://doi.org/10.1088/0004-637X/690/1/L31)
- Pope, M. H., & Melrose, D. B. 1994, *PASA*, 11, 175, doi: [10.1017/S1323358000019858](https://doi.org/10.1017/S1323358000019858)
- Porth, O., Chatterjee, K., Narayan, R., et al. 2019, *ApJS*, 243, 26, doi: [10.3847/1538-4365/ab29fd](https://doi.org/10.3847/1538-4365/ab29fd)
- Rieger, F. M. 2019, *Galaxies*, 7, 78, doi: [10.3390/galaxies7030078](https://doi.org/10.3390/galaxies7030078)
- Rieger, F. M., & Aharonian, F. 2012, *Modern Physics Letters A*, 27, 1230030, doi: [10.1142/S0217732312300303](https://doi.org/10.1142/S0217732312300303)
- Rieger, F. M., & Duffy, P. 2004, *ApJ*, 617, 155, doi: [10.1086/425167](https://doi.org/10.1086/425167)
- . 2006, *ApJ*, 652, 1044, doi: [10.1086/508056](https://doi.org/10.1086/508056)
- . 2019, *ApJL*, 886, L26, doi: [10.3847/2041-8213/ab563f](https://doi.org/10.3847/2041-8213/ab563f)
- . 2022, *ApJ*, 933, 149, doi: [10.3847/1538-4357/ac729c](https://doi.org/10.3847/1538-4357/ac729c)
- Ro, H., Kino, M., Sohn, B. W., et al. 2023, *A&A*, 673, A159, doi: [10.1051/0004-6361/202142988](https://doi.org/10.1051/0004-6361/202142988)
- Schlickeiser, R. 1985, *A&A*, 143, 431
- . 2002, *Cosmic Ray Astrophysics* (Springer Berlin)
- Singh, C. B., Mizuno, Y., & de Gouveia Dal Pino, E. M. 2016, *ApJ*, 824, 48, doi: [10.3847/0004-637X/824/1/48](https://doi.org/10.3847/0004-637X/824/1/48)
- Sironi, L., Rowan, M. E., & Narayan, R. 2021, *ApJL*, 907, L44, doi: [10.3847/2041-8213/abd9bc](https://doi.org/10.3847/2041-8213/abd9bc)
- Skilling, J. 1975, *MNRAS*, 172, 557, doi: [10.1093/mnras/172.3.557](https://doi.org/10.1093/mnras/172.3.557)
- Stawarz, L., & Petrosian, V. 2008, *ApJ*, 681, 1725, doi: [10.1086/588813](https://doi.org/10.1086/588813)
- Tavecchio, F., Costa, A., & Sciacaluga, A. 2022, *MNRAS*, 517, L16, doi: [10.1093/mnras/517/1/L16](https://doi.org/10.1093/mnras/517/1/L16)
- Tavecchio, F., & Ghisellini, G. 2008, *MNRAS*, 385, L98, doi: [10.1111/j.1745-3933.2008.00441.x](https://doi.org/10.1111/j.1745-3933.2008.00441.x)
- Walker, R. C., Hardee, P. E., Davies, F. B., Ly, C., & Junor, W. 2018, *ApJ*, 855, 128, doi: [10.3847/1538-4357/aaafcc](https://doi.org/10.3847/1538-4357/aaafcc)
- Wang, J.-S., Reville, B., Liu, R.-Y., Rieger, F. M., & Aharonian, F. A. 2021, *MNRAS*, 505, 1334, doi: [10.1093/mnras/stab1458](https://doi.org/10.1093/mnras/stab1458)
- Wang, J.-S., Reville, B., Mizuno, Y., Rieger, F. M., & Aharonian, F. A. 2023, *MNRAS*, 519, 1872, doi: [10.1093/mnras/stac3616](https://doi.org/10.1093/mnras/stac3616)
- Webb, G. M., Al-Nussirat, S., Mostafavi, P., et al. 2019, *ApJ*, 881, 123, doi: [10.3847/1538-4357/ab2fca](https://doi.org/10.3847/1538-4357/ab2fca)
- Webb, G. M., Barghouty, A. F., Hu, Q., & le Roux, J. A. 2018, *ApJ*, 855, 31, doi: [10.3847/1538-4357/aaaf6c](https://doi.org/10.3847/1538-4357/aaaf6c)
- Webb, G. M., Xu, Y., Biermann, P. L., et al. 2023, *ApJ*, 958, 169, doi: [10.3847/1538-4357/acfd9](https://doi.org/10.3847/1538-4357/acfd9)
- Wolfram Research, I. 2023, *Mathematica*, Version 13.3. <https://www.wolfram.com/mathematica>
- Yang, H., Yuan, F., Li, H., et al. 2024, *Science Advances*, 10, eadn3544, doi: [10.1126/sciadv.adn3544](https://doi.org/10.1126/sciadv.adn3544)
- Zabalza, V. 2015, *Proc. of International Cosmic Ray Conference 2015*, 922
- Zech, A., & Lemoine, M. 2021, *A&A*, 654, A96, doi: [10.1051/0004-6361/202141062](https://doi.org/10.1051/0004-6361/202141062)